Pure appl. geophys. 159 (2002) 247–276
0033–4553/02/030247–30 $ 1.50 + 0.20/0

Pure and Applied Geophysics

Modelling Seismic Waves Around Underground Openings in Fractured Rock

MARK WILLIAM HILDYARD[1] and R. PAUL YOUNG[2]

Abstract — The potential for large excavation-induced seismic events may be recognised, even if the timing of an event may be inherently unpredictable. In this case, modelling the wave propagation from a potential event could allow the dynamic motions around an excavation to be projected, and for areas of danger to be anticipated. However, the above and other potential applications require accurate models of wave interaction with the openings, as well as with the fractured rock which surrounds such excavations. This paper considers real recorded waveforms and how well these waveforms are modelled by explicit mechanical models of the source, the medium and the excavation. Models of experiments at three different scales of the problem are presented: small and large amplitude waveforms recorded around a deep-level mining tunnel in a synthetic rockburst experiment; waveforms from laboratory experiments of waves through plates of steel representing fractures; waveforms from active pulses in an acoustic emission experiment in a small volume of fractured rock at the surface of an underground excavation. The results show that elastic wave propagation around an excavation was a first approximation for small amplitude waves, but was less successful for modelling large amplitude waves and more fractured rock. Fractures in the models were represented explicitly with displacement discontinuities. Waveforms through known fracture geometries were particularly well-reproduced, and indicate the importance of fracture stiffness, the *in situ* stress state, and stress-dependence of the fractures in such models. Overall, the models are sufficiently successful at representing recorded behaviour, to be encouraging for the goal of representing accurate wave motions around excavations.

Key words: Wave, model, seismic, rock, rockburst, fracture.

1. Introduction

Rockbursts and seismicity in mines is a serious hazard and is widespread in the deep hard-rock mining districts of the world. Large numbers of induced seismic events occur in deep mines, many of which are potentially damaging. Although attempts are made to forecast such damaging events (MENDECKI, 1993), it is not in general possible to predict when damaging events will occur. Even knowing the location of a potential

[1] Department of Earth Sciences, Jane Herdman Laboratories, 4 Brownlow Street, University of Liverpool, Liverpool L697GP, United Kingdom. E-mail: mwh@liv.ac.uk and CSIR Division of Mining Technology, P.O. Box 91230, Auckland Park, 2006, Johannesburg, South Africa.
E-mail: mhildyar@csir.co.za
[2] Department of Earth Sciences, Jane Herdman Laboratories, 4 Brownlow Street, University of Liverpool, Liverpool L697GP, United Kingdom.

event, it is not obvious whether the event will cause damage and which regions of the excavation will be damaged. It is often reported that damage can occur quite distant from the source and in unexpected areas. This may be due to the influence of the excavation on wave propagation, as is illustrated by the example in Figure 1. If wave propagation could be modelled around excavations, then it may be possible to anticipate regions of likely damage for potential events. This could be used as important feedback into the safety design process.

The ability to model wave propagation around deep underground openings therefore has important potential applications affecting the design and stability of such openings. This is true both for mining where short-term stability is required, as well as for other fields such as nuclear waste disposal requiring extremely long-term

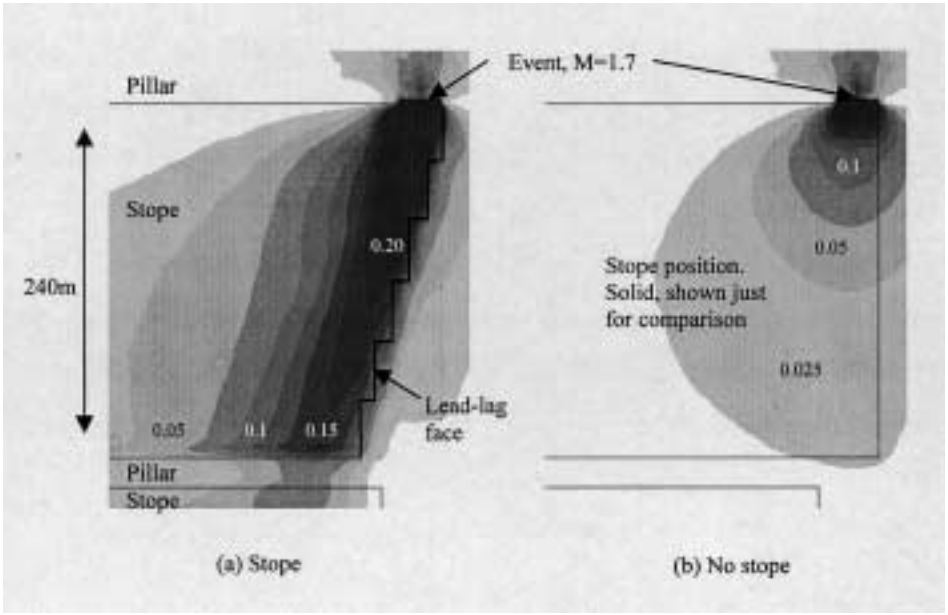

Figure 1

The projected influence of a mining layout on the wave propagation from a seismic event. Plan sections are shown through two three-dimensional elastic models, one containing a tabular mining excavation, the other a purely solid material. The contours indicate the maximum vertical velocity (in m/s), induced by a particular seismic event of magnitude 1.7, for a plane just below the excavation. The mining layout consists of a lead-lag stope, where the stope is a narrow excavations of 1.5 meters height but extending for hundreds of metres. Pillars are regions which have not been excavated, for stability reasons. The 'stepped' outline shows the mining face position or lead-leg face. The event was assumed to occur in a pillar parallel to the direction of mining advance, and just behind the face position of the mining. Further details regarding, the source are given in Appendix A, Section 1. The influence of the stope on the wave propagation causes velocities at a far pillar to be up to six times that of the solid model without the excavaion. This is due to wave propagation along the free surface, and the influence of the mining face. The above layout and spans of open excavation are quite typical in certain tabular mines (e.g., HANDLEY *et al.*, 1997; MALAN (1999); JAGER and RYDER, 1999).

stability. Such models allow studies to be made of the influence of a particular excavation on the wave propagation and distribution of peak motions, and on mechanisms that can lead to larger motions than expected. Furthermore if models can reproduce the wave propagation around the openings, then the likely motions and amplitudes could be projected for potential events. This would allow regions of likely damage to be identified, and for appropriate design action to be taken. Yet another possibility is that since the waves pass through fractured rock, matching recordings with models may provide information on the state of the rock at the skin of the excavation.

One feature of deep underground excavations is a highly fractured rock mass. This excavation-induced damage may extend many metres into the rockmass (e.g., ADAMS and JAGER, 1980; NAPIER *et al.*, 1997), complicating wave behaviour, and the task of modelling wave propagation. A wide body of literature deals with studies of waves through fractured rock. A displacement discontinuity has been investigated as a discrete representation of a fracture (SCHOENBERG, 1980; MYER, 1985), while experimental studies have indicated that this representation captures some of the frequency effects on waves due to fracturing (PYRAK-NOLTE *et al.*, 1990a, b). Numerical studies using this representation have tended to be made with assumptions of plane waves, two-dimensional modelling, or contain very limited numbers of fractures (e.g., GU *et al.*, 1996; CAI and ZHAO, 2000). Another approach attempts to encapsulate the effects of numerous fractures into the behaviour of the medium, in particular in terms of the effective wave-speed, but also attenuation effects (e.g., O'CONNELL and BUDIANSKY, 1974; SAYERS and KACHANOV, 1991; LIU *et al.*, 2000). These approaches assume low frequency. Most numerical studies of waves through fractures therefore make some of the following assumptions: two-dimensional wave propagation, plane wave propagation, small amplitude motions, low frequency relative to crack size, dilute crack concentration, uniform stress state. Many of these assumptions are poor in the context of real problems involved with wave propagation around underground openings. Excavations are firstly in a highly non-uniform stress field. In the case of deep-level mining, the excavation surface is highly fractured, wave amplitudes may be large, and sources are in the near-field and non-planar, while the full length of dynamic motion is important, and not just the initial arrivals. Microseismic and ultrasonic recordings used to monitor excavations and infer rock-mass state, include frequencies which do not satisfy low frequency or plane wave assumptions.

This paper begins to redress some of these deficiencies, by applying fully three-dimensional, full-wave modelling to waves recorded in excavations and through fractures. The modelling is unique in terms of the type and scale of problem to which it is applied.

Three case studies are reported covering different scales and aspects of the problem. The first study considers a real excavation problem, modelling both small and large amplitude waves originating in the near-field of a mine tunnel. The data

modelled is from a rockburst experiment, where an artificial source was used to generate large amplitude, damaging seismic waves. Results cover attempts to model the waveforms with a purely elastic rock mass, although models with fractures were also examined. The second case study compares models with a laboratory experiment, where waves were passed through stacked steel plates, with the plate-to-plate boundaries representing fractures. The measured waveforms are reproduced in detail by the model, and the importance of the loading on the behaviour of the fractures is studied. The results demonstrate that this model of a fracture captures the essence of the wave behaviour. The third case study extends the successes of these fracture models to an unknown distribution of fractures in rock surrounding an excavation, nonetheless still with the advantages of a controlled and small-scale experiment. The data were recorded in velocity surveys from an acoustic emission experiment, performed in an underground tunnel as part of research into nuclear waste disposal. The modelling attempts to account for the recorded amplitudes and velocities of waveforms, relative to that expected in unfractured rock. The work touches on a second application requiring accurate models, which aids in interpreting the fracture state of the rock through which waves have passed.

2. Methodology

The cases studied in this paper intend to provide a measure of the ability of elastodynamic models to predict full wave propagation around openings and in fractured rock. Results are obtained by forward modelling using a known geometry and source. In all cases there are aspects of the source and geometry which are unknown. An effort is made to keep these assumptions physically reasonable and mechanistic. For example, it is possible to manipulate the spatial and time distribution of source in an attempt to better match recorded data. Instead, an important assumption is made that the source is a simple function, and that complexity is introduced by the geometry and fractures in the medium.

A number of different numerical methods exist for modelling elastodynamic behaviour, including variations of boundary element, finite element, finite difference and pseudo-spectral techniques. This work is performed with a finite difference model using the program WAVE (CUNDALL, 1992; HILDYARD *et al.*, 1995). One of the advantages is the size of three-dimensional problems which can be studied, including multitudes of fractures. The method used solves the coupled system of first-order equations obtained from the equation of motion, and the material constitutive equations relating stress and strain. The volume of interest is discretised on a staggered grid (c.f. Fig. 2), and the equations are solved using an explicit time-marching scheme. This approach is widely used for modelling seismic wave propagation (e.g., MADARIAGA, 1976; VIRIEUX, 1986; GRAVES, 1996), in part due to its computational efficiency. This efficiency is primarily due to it been readily

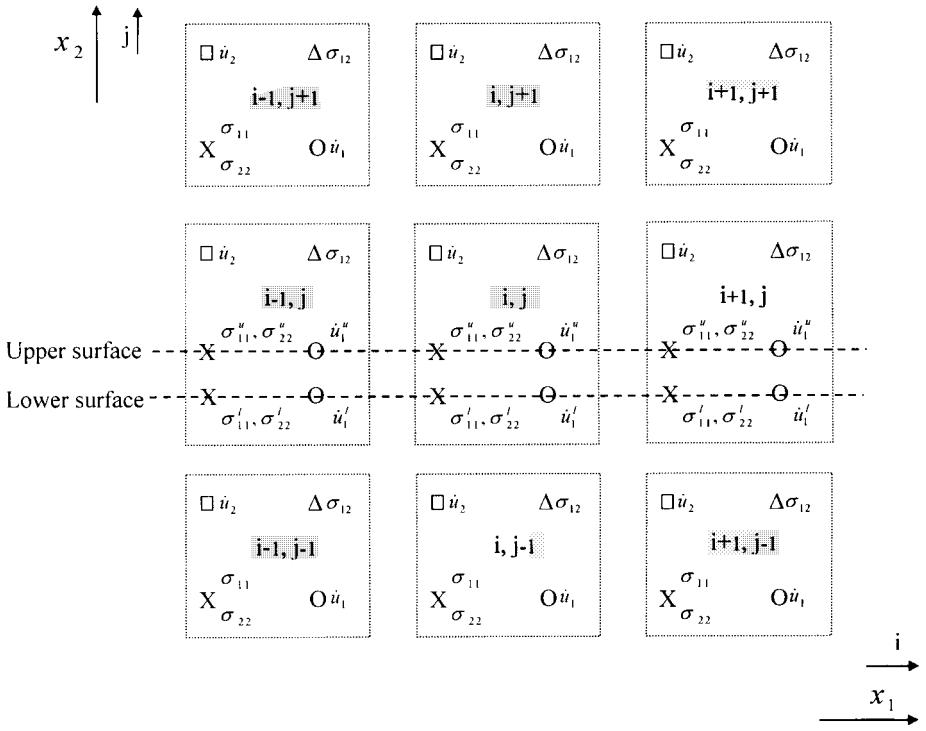

Figure 2
Portion of a two-dimensional staggered mesh showing the spatial distribution of components of velocity and stress. Representation of a two-dimensional horizontal crack shows surrounding grid variables and the appropriate dual-valued grid variables on the surfaces.

extendible to give higher order spatial accuracy (LEVANDER, 1988). The models are solved to fourth-order spatial accuracy, and second-order time accuracy.

Dynamic sources are implemented by prescribing the velocity or stress on grid-points. All boundaries impose absorbing conditions based on LYSMER and KUHLEMEYER (1969). Certain models solve the coupled problem of a static stress load with a transitory dynamic load. In these cases the static solution is first obtained through asymptotic solution of the wave equations to applied stresses at the boundaries, and by applying viscous damping in the mesh.

The main features used in the models in this paper are openings and cracks. Cracks are represented by displacement discontinuities, which are implemented by splitting a surface in the mesh into two coincident surfaces, each with its own set of grid-points (c.f. Fig. 2). Boundary conditions are enforced on these surfaces. The crack can be open, behaving like separate free surfaces which can interpenetrate, or coupled by a normal and shear fracture stiffness, which relate the normal and shear stress at the crack surfaces to the relative normal and tangential displacement of

the crack surfaces. Other conditions such as tensile failure or frictional sliding were not used in the reported models. The surfaces are welded at the crack edges and behave as solid material. Openings are represented using open cracks. Narrow openings are modelled as a single open crack, while wide openings such as tunnels are modelled by enclosing a volume with open cracks, and isolating the enclosed grid-points.

HILDYARD *et al.* (1995) and NAPIER *et al.* (1997) contain previous applications of the two-dimensional code, including verification through comparison with photo-elastic experiments of wave interaction with openings and interfaces. We now derive selected grid and crack equations for three-dimensions (based on CUNDALL, 1992).

The method solves for velocity and stress on a staggered mesh, with the different components held at different positions in space (Fig. 2). Consider first a continuous solid mesh without any cracks. The time derivatives of the constitutive equations for a linear elastic isotropic material are:

$$\dot{\sigma}_{ij} = \delta_{ij}\left(K - \frac{2}{3}G\right)\dot{e}_{kk} + 2G\dot{e}_{ij}, \quad \text{where } \dot{e}_{ij} = \frac{1}{2}\left[\frac{\partial \dot{u}_i}{\partial x_j} + \frac{\partial \dot{u}_j}{\partial x_i}\right] \ , \tag{1}$$

where K is the bulk modulus, G is the shear modulus, δ_{ij} is the Kronecker delta, σ_{ij} are components of the stress tensor, e_{ij} are components of the strain tensor, $\dot{u}$ is velocity, and a dot indicates a time derivative. Applying equation (1) at the σ_{22} position in cell (i,j) (assumed here to be in solid material), and approximating using second-order central finite differences, gives

$$\sigma_{22}^{t} = \sigma_{22}^{t-1} + E_1\frac{\Delta t}{\Delta x_2}\left(\dot{u}_2^{j} - \dot{u}_2^{j-1}\right)^{t-1/2} + E_2\frac{\Delta t}{\Delta x_1}\left(\dot{u}_1^{i} - \dot{u}_1^{i-1}\right)^{t-1/2} + E_2\frac{\Delta t}{\Delta x_3}\left(\dot{u}_3^{k} - \dot{u}_3^{k-1}\right)^{t-1/2} \tag{2}$$

where $E_1 = K + 4G/3, E_2 = K - 2G/3$. Superscripts i, j or k represent the spatial direction for the differencing, while superscript t indicates discrete time. A new value of σ_{22} at time t is calculated from σ_{22} at time $t-1$, and velocities at time $t-1/2$, so that velocities are staggered in time by $\Delta t/2$ with respect to stresses. Similar expressions are obtained for the five remaining stress components.

The equations of motion excluding body force are:

$$\rho\frac{\partial \dot{u}_i}{\partial t} = \frac{\partial \sigma_{ij}}{\partial x_j} \tag{3}$$

where ρ is density and $\dot{u}$ is velocity. Applying equation (3) at the $\dot{u}_2$ position in cell (i, j) in the staggered mesh, and approximating using second-order central finite differences, gives

$$\dot{u}_2^{t+\frac{1}{2}} = \dot{u}_2^{t-\frac{1}{2}} + \frac{1}{\rho}\frac{\Delta t}{\Delta x_2}\left(\sigma_{22}^{j+1} - \sigma_{22}^{j}\right)^{t} + \frac{1}{\rho}\frac{\Delta t}{\Delta x_1}\left(\sigma_{12}^{i} - \sigma_{12}^{i-1}\right)^{t} + \frac{1}{\rho}\frac{\Delta t}{\Delta x_3}\left(\sigma_{23}^{k} - \sigma_{23}^{k-1}\right)^{t} \ . \tag{4}$$

Similar expressions are obtained for the two remaining velocity components. Equations (2) and (4) and the related equations for other components provide the nine basic second-order grid equations for the solid material. Higher order spatial differencing is introduced by including more distant terms.

We now introduce a horizontal discontinuity into the mesh as illustrated for two dimensions in Figure 2. This consists of two coincident surfaces on which certain grid variables are controlled, and others allowed to be dual-valued. The grid variables locating on the crack surfaces have an upper and lower value i.e., σ^u_{22}, σ^l_{22}, σ^u_{11}, σ^l_{11}, σ^u_{33}, σ^l_{33}, σ^u_{13}, σ^l_{13}, $\dot{u}^u_1$, $\dot{u}^l_1$, $\dot{u}^u_3$ and $\dot{u}^l_3$. From continuity $\sigma^u_{22} = \sigma^l_{22} = \sigma_{22}$. However σ_{11}, σ_{33}, σ_{13}, $\dot{u}_1$ and $\dot{u}_3$ are dual-valued, and values for the upper and lower surfaces must be independently calculated. From equation (2) we can write two separate mesh equations for $\Delta\sigma_{22}$, which is the increment required to update σ_{22} from time-step t to $t + 1$, (for convenience, we now drop the t superscript notation), giving

$$\Delta\sigma^u_{22} = E_1 \frac{\Delta t}{\Delta x_2}(\dot{u}^j_2 - \dot{u}^{(uf)}_2) + E_2 \frac{\Delta t}{\Delta x_1}(\dot{u}^{i(u)}_1 - \dot{u}^{i-1(u)}_1) + E_2 \frac{\Delta t}{\Delta x_3}(\dot{u}^{k(u)}_3 - \dot{u}^{k-1(u)}_3) \tag{5}$$

$$\Delta\sigma^l_{22} = E_1 \frac{\Delta t}{\Delta x_2}(\dot{u}^{(lf)}_2 - \dot{u}^{j-1}_2) + E_2 \frac{\Delta t}{\Delta x_1}(\dot{u}^{i(l)}_1 - \dot{u}^{i-1(l)}_1) + E_2 \frac{\Delta t}{\Delta x_3}(\dot{u}^{k(l)}_3 - \dot{u}^{k-1(l)}_3) \tag{6}$$

where $\dot{u}^{(uf)}_2$ and $\dot{u}^{(lf)}_2$ are "fictitious" quantities, since $\dot{u}^{(uf)}_2$ falls below the upper surface and $\dot{u}^{(lf)}_2$ is above the lower surface of the crack. We now assume that the normal stress on the crack surface is coupled to the relative normal displacement by a linear stiffness k_n, such that

$$\Delta\sigma_{22} = \dot{u}^{\text{rel}}_2 k_n \Delta t = k_n \Delta t \left[\frac{\dot{u}^j_2 + \dot{u}^{(uf)}_2}{2} - \frac{\dot{u}^{j-1}_2 + \dot{u}^{(lf)}_2}{2}\right]. \tag{7}$$

Combining equations (5), (6) and (7), the fictitious stresses $\dot{u}^{(uf)}_2$ and $\dot{u}^{(lf)}_2$ are eliminated, giving

$$\Delta\sigma_{22} = E_1 \frac{E_1 k_n \Delta t}{E_1 + k_n \Delta x_2}\left[\left(\dot{u}^j_2 - \dot{u}^{j-1}_2\right) + \frac{1}{2}\frac{E_2}{E_1}\frac{\Delta x_2}{\Delta x_1}\dot{u}^{\text{diff}}_1 + \frac{1}{2}\frac{E_2}{E_1}\frac{\Delta x_2}{\Delta x_3}\dot{u}^{\text{diff}}_3\right] \tag{8}$$

where

$$\dot{u}^{\text{diff}}_1 = \dot{u}^{i(u)}_1 - \dot{u}^{i-1(u)}_1 + \dot{u}^{i(l)}_1 - \dot{u}^{i-1(l)}_1 \tag{9}$$

where

$$\dot{u}^{\text{diff}}_3 = \dot{u}^{k(u)}_3 - \dot{u}^{k-1(u)}_3 + \dot{u}^{k(l)}_3 - \dot{u}^{k-1(l)}_3 \tag{10}$$

σ^u_{11}, σ^l_{11}, σ^u_{33} and σ^l_{33} can then be calculated using

$$\Delta\sigma^u_{11} = \frac{2G(6K + 2G)\Delta t}{(3K + 4G)\Delta x_1}(\dot{u}^{i(u)}_1 - \dot{u}^{i-1(u)}_1) + \frac{2G(3K - 2G)\Delta t}{(3K + 4G)\Delta x_3}(\dot{u}^{k(u)}_3 - \dot{u}^{k-1(u)}_3) + \frac{E_2}{E_1}\Delta\sigma_{22} \tag{11}$$

$$\Delta\sigma_{11}^{l} = \frac{2G(6K+2G)\Delta t}{(3K+4G)\Delta x_1}\left(\dot{u}_1^{i(l)} - \dot{u}_1^{i-1(l)}\right) + \frac{2G(3K-2G)\Delta t}{(3K+4G)\Delta x_3}\left(\dot{u}_3^{k(l)} - \dot{u}_3^{k-1(l)}\right) + \frac{E_2}{E_1}\Delta\sigma_{22} \tag{12}$$

$$\Delta\sigma_{33}^{u} = \frac{2G(3K-2G)\Delta t}{(3K+4G)\Delta x_1}\left(\dot{u}_1^{i(u)} - \dot{u}_1^{i-1(u)}\right) + \frac{2G(6K+2G)\Delta t}{(3K+4G)\Delta x_3}\left(\dot{u}_3^{k(u)} - \dot{u}_3^{k-1(u)}\right) + \frac{E_2}{E_1}\Delta\sigma_{22} \tag{13}$$

$$\Delta\sigma_{33}^{l} = \frac{2G(3K-2G)\Delta t}{(3K+4G)\Delta x_1}\left(\dot{u}_1^{i(l)} - \dot{u}_1^{i-1(l)}\right) + \frac{2G(6K+2G)\Delta t}{(3K+4G)\Delta x_3}\left(\dot{u}_3^{k(l)} - \dot{u}_3^{k-1(l)}\right) + \frac{E_2}{E_1}\Delta\sigma_{22} \ . \tag{14}$$

Expressions for updating velocities $\dot{u}_1^u$, $\dot{u}_1^l$, $\dot{u}_3^u$ and $\dot{u}_3^l$ are calculated in a similar manner, by assuming that the surface shear stress and relative shear displacement are coupled by a linear stiffness k_s. i.e., by writing expressions for $\dot{u}_1^u$ and $\dot{u}_1^l$ using fictitious grid-points, and using the condition

$$\Delta\sigma_{12}^{\text{surf}} = \dot{u}_1^{\text{rel}} k_s \Delta t = k_s \Delta t\left(\dot{u}_1^u - \dot{u}_1^l\right) \tag{15}$$

where $\Delta\sigma_{12}^{\text{surf}}$ locates on the crack surface which is not a normal grid position for σ_{12}. Noting that σ_{12} is continuous across the crack, all fictitious points can be eliminated. The remaining crack values σ_{13}^u and σ_{13}^l can be calculated simply by ensuring that the velocities from the correct sides of the crack are used in the difference calculations. The special case of an open crack, with free surface conditions on both surfaces, is obtained by setting $k_n = 0$ and $k_s = 0$. Edge conditions are required at the ends of the crack to match the dual-valued crack calculations to the standard mesh calculations.

3. A Case Study: Modelling Seismic Waves from a Rockburst

This first section concerns the accuracy of wave modelling at the excavation-size scale for both small and large amplitude waves. It covers a case study from a real excavation. The data were obtained in an experiment to simulate a rockburst in a deep-level underground tunnel.

Although back-analysis of seismic events is widespread in studies of large earthquakes, sparse published work has attempted to apply numerical models to back-analyse the wave motions around underground openings due to rockbursts (e.g., HANDLEY *et al.*, 1996). Certain factors should be highlighted which contribute to the complexity of this task. The proximity of the excavation to the source means that waves begin to interact with the excavation before far-field conditions are reached. Fractured or damaged zones associated with deep excavations lead to more complex wave interactions. Finally, the primary interest is motion at the excavation surface so that meaningful back-analysis requires recordings within the excavation. In this case a simulated event is studied. The advantage of examining a simulated

event rather than a natural event is *a priori* knowledge of the source and the excavation layout and condition, and the chance to prepare and receive good coverage of recordings, particularly at the surfaces of excavations.

The artificial rockburst experiment was performed in an underground tunnel at a deep-level gold mine in South Africa. The purpose of the experiment was to create and extensively monitor a controlled seismic event, and to induce and observe seismic damage in a nearby tunnel (MILEV *et al.*, 2000). Extensive numerical modelling of seismic wave propagation was used in the experiment (HILDYARD and MILEV, 1999). The forward analysis included the development of a source model for a propagating blast and the modelling of data from a small calibration blast. The back analysis applied the source model to data from the main experiment. Here however, we concentrate exclusively on the comparisons between the modelled waveforms and recordings for both large amplitude and small amplitude waves recorded in the experiment.

The experiment took place in a tunnel at a depth of 1600 m. The tunnel had an approximately square shape and relatively unfractured walls. A small (0.67 kg) calibration blast was made at one end of the tunnel, close to the tunnel surface. The main experiment was a larger (260 kg) explosion at the opposite end of the tunnel, comprised of five separate blastholes of 4 m to 7 m in length, deep in solid rock 6 metres away from the tunnel. Thirty-two geophones were in place with a sampling rate of 10 kHz and low-pass filtering from 750 Hz. For the main blast, three accelerometers were positioned on the tunnel surface where the largest motions were expected. These had a sampling rate of 500 kHz. Prior to the blast, fractures on the tunnel wall were mapped to determine the rock-mass state. The beddings were spaced between 150 mm and 600 mm and were generally closed. Joints were spaced between 0.5 m and 3.0 m, and were closed. Stress fractures associated with the development of the tunnel were generally open by up to 2 mm with a spacing of approximately 10 cm, and intersections defined wedge-shaped blocks (REDDY and SPOTTISWOODE, 2000).

The tunnel was modelled as a square cavity with a side of 3.6 metres, and 37 metres long. Figure 3 shows the model geometry and positions of the geophones and accelerometers used in comparisons. These were uniaxial and mounted along the surface of the near tunnel wall. A typical model used 800,000 grid-points with a 0.2 metre spacing, and fourth-order spatial differencing. Model details are given in Appendix A for Section 3.

The calibration blast had a 0.037 m diameter, a 0.65 m charge length, a 0.67 kg charge mass, and a detonation velocity of 4500 m/s. It was one metre from the tunnel and inclined away from the geophones at 75 degrees (nearly normal) to the tunnel surface. Figure 4 compares the modelled velocity seismograms with those recorded at varying distances along the tunnel near wall. The model is elastic and represents only the source, and the effect of the opening. Scales are the same for corresponding waveforms. The motions match well in a qualitative sense. In both cases the *P* wave is lower amplitude than the *S* wave, particularly with greater distance. Amplitudes are similar, and the decay with distance of both the *P* and the *S* waves is well modelled.

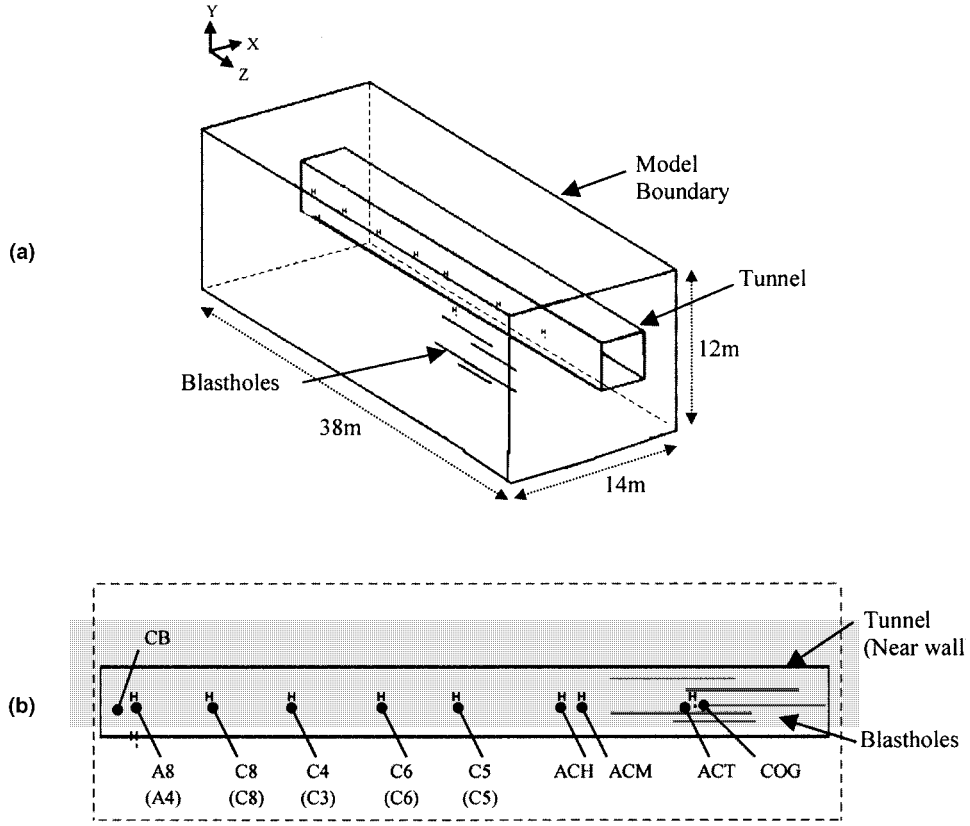

Figure 3
Model geometry for the rockburst experiment. (a) 3-D sketch, (b) front view showing positions of some of the geophones and accelerometers. 'COG' is the approximate centre of the main blast. 'CB' is the calibration blast. 'ACT', ACM' and 'ACH' are accelerometer positions, while other marked positions are geophones. Labels given in brackets are geophone positions for the calibration blast.

Arrivals are slightly quicker in the data, indicating faster wave speeds. At positions where triaxial data were available, not all components were well-matched.

The main experiment was designed to generate peak particle velocities in the tunnel of around 3 m/s, without any direct damage at the tunnel due to gas expansion. Five synchronous blasts were used to generate a large enough source. The five blastholes varied widely, but were approximately 6 metres from the tunnel, parallel to the tunnel, and vertically spaced with a spacing of 0.5 m. The diameter was 0.1 m, the average charge length 6 m, and the detonation velocity 3600 m/s, with detonation staggered by 70 μs for each blast-hole. The total charge mass was 260 kg of Anfo explosive. A number of the geophones were overdamped for the main experiment to allow recording of strong ground motion (MILEV *et al.*, 2000). In spite of the advantages of a known source position, considerable uncertainty exists for

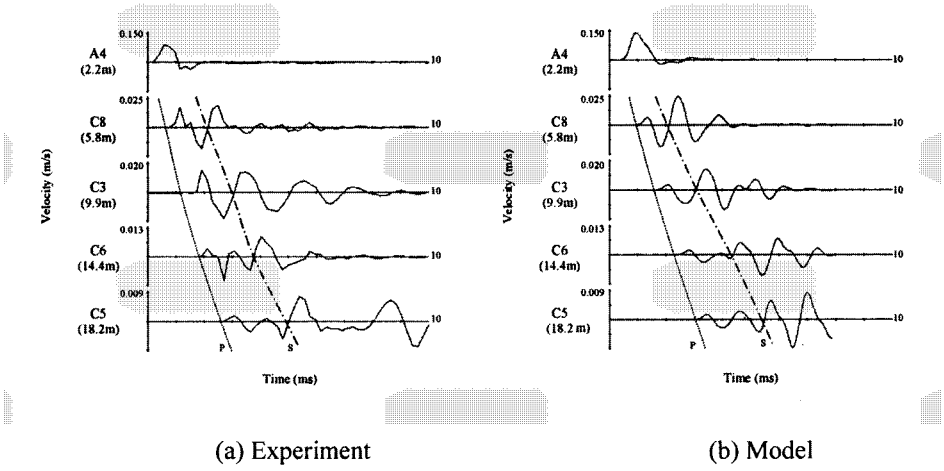

Figure 4
Comparison of velocity seismograms for the calibration blast at varying distances along the tunnel near wall. Positions for geophones A4, C8, C3, C6, C5 are shown in brackets in Figure 3. Motion is normal to the tunnel surface. Approximate *P*-wave arrivals, and the position of secondary waves (not the *S*-wave arrival), are indentified.

wave propagation from a detonating rather than an instantaneous blast, and much of the modelling involved developing a suitable source model. A mechanistic representation of the source was used to account for the slow detonation, and because the proximity of the tunnel makes near-field wave propagation important. The source model involved a pressure propagating along the line of the blast hole at the velocity of detonation of the blast. Initial models assumed an elastic rock mass. Figure 5 compares the waveforms recorded at various distances along the surface of the tunnel near-wall for the experiment and for the model, respectively. The positions of these recordings are shown in Figure 3.

Considering firstly just the *P*-wave portion of the waveforms, Figure 5 shows that the model at least matches the data in the direction of the first motions. However, in the data the width of the first pulse varies between successive positions, and in fact there is little similarity in waveforms between successive recordings. In contrast, the modelled waveforms vary smoothly with distance. Moreover, Figure 6a shows that the *P*-wave amplitude decays smoothly in the model, while the decay is not monotonic in the data. Comparing Figure 5a with Figure 4a, the change and decay of waveforms with distance is also less coherent than that for small amplitude waves in the calibration blast. The waves therefore do not decay or change in the manner predicted by elastic wave propagation. The data set is small so this may simply reflect errors in the data due to the difficulty of recording large amplitude ground motion accurately. Two problems could lead to such errors in the data; either poor coupling, or the unusual damping where larger than normal resistors were used in the

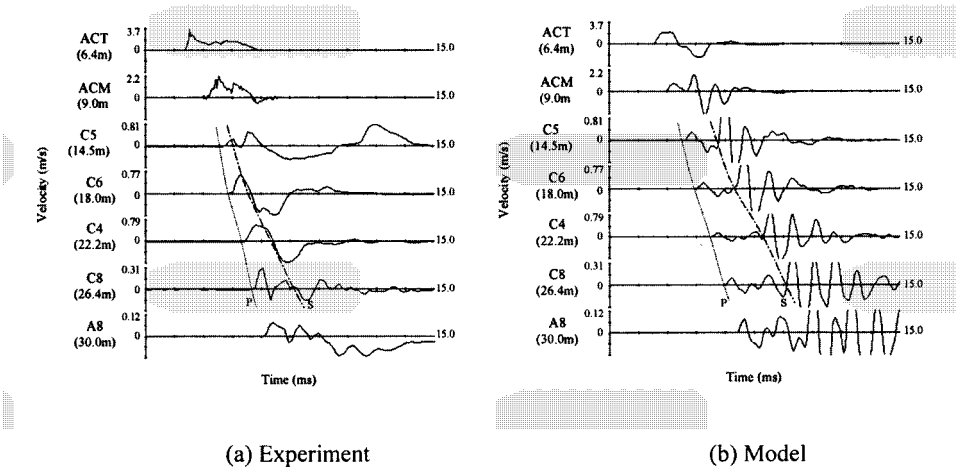

Figure 5
Comparison of velocity seismograms for the main blast at varying distances along the tunnel near wall. Positions for accelerometers ACT and ACM, and geophones A8, C5, C6, C4 and C8 shown in Figure 3. Motion is normal to the tunnel surface. Approximate *P*- and *S*-wave arrivals are shown. ACT and ACM were integrated from accelerometer data. Recordings for ACT, ACM and A8 were not on the same time-base, and have been time-shifted to their probable arrival time relative to C5.

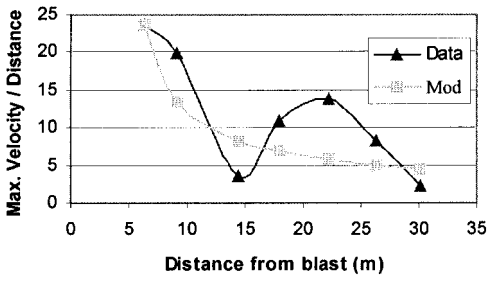

Figure 6
Decay in particle velocity with distance from the source for the recorded and modelled waveforms. The graph shows the amplitude of the first arrival scaled by distance from the source.

geophones to cope with velocities of up to 1 m/s (MILEV *et al.*, 2000). No physical evidence of poor coupling was reported for these geophones. Instead, the lack of coherence in the measured waveforms may indicate differences in the fracture state near geophones, and the differences in wave propagation for large amplitude waves. Such differences would occur due to the waves generating damage, or interacting with existing damage, or changing the loading and hence the rock properties. Although the recordings after accelerometer ACM were beyond the region of observed damage, the particle velocity in this region was still between 0.3 m/s and 0.81 m/s, inducing significant transitory stress changes.

The most fundamental difference in waveforms in Figure 5 is that the secondary waves in the model are much larger than the initial *P* wave, in contrast to the measured waveforms in which secondary waves were mostly of the same order as the initial arrivals. These differences could be poor source modelling. The large secondary waves in the model are in fact Rayleigh waves which develop due to large incident shear waves. This is a direct result of the source model for a propagating blast, which has been shown to generate large shear waves for a low detonation velocity (DAEHNKE, 1997; KOUZNIAK and ROSSMANITH, 1998). The source model is primarily based on theoretical rather than physical evidence, and physical evidence is required to confirm whether a shear wave can be expected at a distance from the blast. If the source model is valid, then an alternative explanation is that the differences again relate to the generation of or the opening of fractures. A model which allowed tensile failure on fractures near the tunnel surface was shown to reduce the relative content of the secondary waves by impeding development of a Rayleigh wave (HILDYARD and MILEV, 1999).

Two indicators from the model: maximum velocity and maximum induced tensile stress, were compared with regions of recorded damage. Unfortunately, these include the influence of the anomalously large secondary waves which make comparison somewhat misleading. Figure 7 compares the modelled maximum induced tensile stress for the near wall of the tunnel with recorded damage. Regions marked 'H' and 'L' indicate areas where high and low intensity damage was reported. Induced stress in σ_{yy} is concentrated opposite the blast holes (maximum 25 MPa) with a maximum of 10 MPa ahead of the blast. The induced tensile stress in σ_{zz} is also high opposite the blast holes (maximum 25 MPa), but there is a second highly tensile region ahead of the blast on the edge of the low intensity damage zone. The above stresses could lead to tunnel normal fracturing, however they should be seen in the context of the total stress state.

The above illustrates the value of accurate wave models. If real waveforms are known to be well-matched, then the model provides detail over a region, including induced stress state, which is not directly known from measurements. The waveforms in this case study however, are not sufficiently well-matched to infer such information. Notably, differences were observed between small and large amplitude waves. Modelling the small amplitude waves proved fairly successful with an elastic material, while modelling the large amplitude waves was not. Interaction with fracturing may account for these differences. The modelling of fractures is examined in the next sections.

4. Wave Propagation through Fractures – Laboratory Experiments

As has been discussed, one of the complications in modelling waves around deep excavations in a rock mass, is that the rock surrounding such openings is fractured.

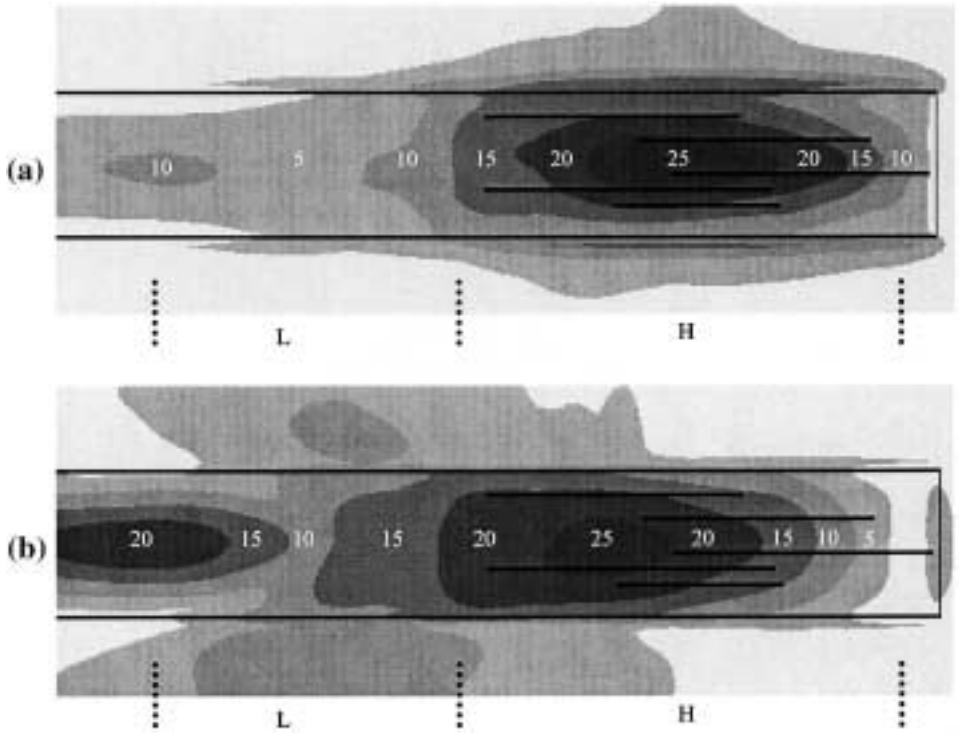

Figure 7
Distribution of maximum induced tensile stress (in MPa) at the tunnel near wall, for the 8 ms source, and for stress components (a) σ_{yy}, vertical, and (b) σ_{zz}, parallel to the tunnel. (i.e., the maximum recorded at a position over all time). Positions 'H' and 'L' show the regions where high and low intensity damage was reported in the experiment.

One approach to account for fracturing is to consider the fractured rock as an effective elastic medium, in which the elastic constants are related to the density of fracturing, typically leading to anisotropy in the seismic velocities (e.g., O'CONNELL and BUDIANSKY, 1974; CRAMPIN, 1981; SAYERS and KACHNOV, 1991). Expressions for the effective attenuation can also be calculated (HUDSON, 1981; LIU *et al.*, 2000). The main restriction is that this is valid only for wave propagation of wavelength considerably greater than the fracture size, although there are also restrictions on the density of fracturing.

An alternative approach is to model each fracture or group of fractures explicitly. A displacement discontinuity is such a model, where the displacements of the two surfaces of a zero-thickness interface are discontinuous, and the difference in displacements of the two surfaces is related to the stress across the interface. The stress and the discontinuity in displacement across the two surfaces are coupled by a fracture stiffness. This has been studied as a representation of a fracture (SCHOENBERG, 1980; MYER *et al.*, 1985), and shown to be consistent with experiments on

natural dry fractures in rock, in terms of the frequency dependence of both wave speed and attenuation (PYRAK-NOLTE *et al.*, 1990a).

For modelling potentially damaging waves around underground openings, models of explicit fracturing seem attractive, as the effect of waves on the fractures can also be studied. This section evaluates the accuracy of fracture models based on the displacement discontinuity, by modelling experiments from PYRAK-NOLTE *et al.* (1990b). The experiments recorded waveforms for both *P* and *S* waves passed through a stack of parallel steel plates, representing a parallel set of fractures. Transmitting and receiving transducers contained both *P*- and *S*-wave piezoelectric elements of 22 mm diameter. Thirty-one mild steel plates were stacked to form a cube with a side of 90 mm. The plates were sandblasted before being stacked, to simulate fracture surfaces. The block was biaxially loaded with a force of 30 kN – one load clamping the plates and a second equal load parallel to the plates. A solid cylinder with an axis of 99 mm provided an unfractured control case. Figure 8a shows a schematic of the experiment.

This experiment was modelled in three dimensions, details of which are given in Appendix A, Section 4. *P*- and *S*-wave sources were inverted from the waveform through the unfractured cylinder, and these sources were then used for the fracture cases. Three *P*-wave cases and four *S*-wave cases were modelled, initially with fractures with uniform fracture stiffness of 6el3 Pa/m and 2el3 Pa/m for the normal and shear directions, respectively.

Figure 9 presents the comparison for *P*-wave transmission. Wave propagation parallel to the fractures (9c) results in a completely different waveform from that of

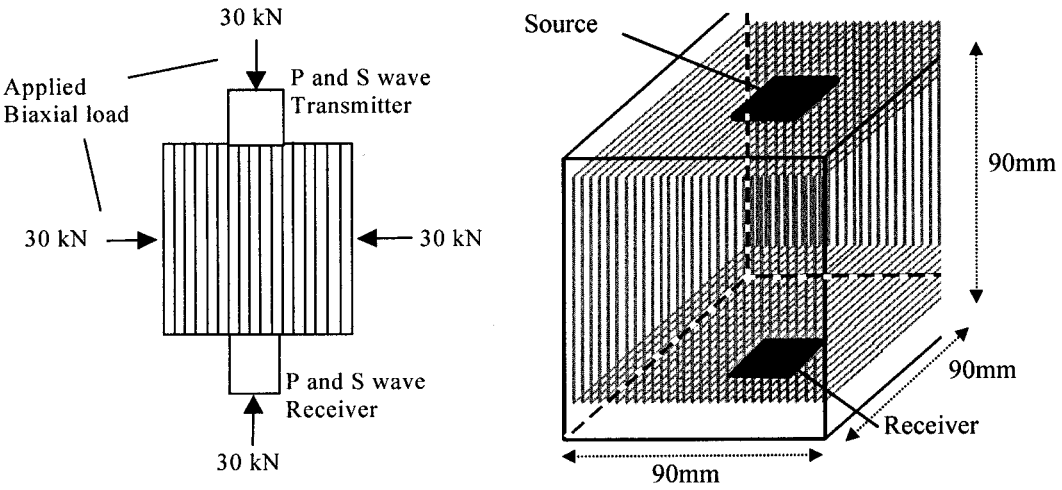

Figure 8

Sketch of the multiple fracture experiment. (a) The experimental system of packed steel plates, transmitter and receiver transducers, and bi-axial loading. (reproduced for PYRAK-NOLTE *et al.*, 1990b). (b) The 3-D WAVE model with displacement discontinuities representing interfaces between the steel plates.

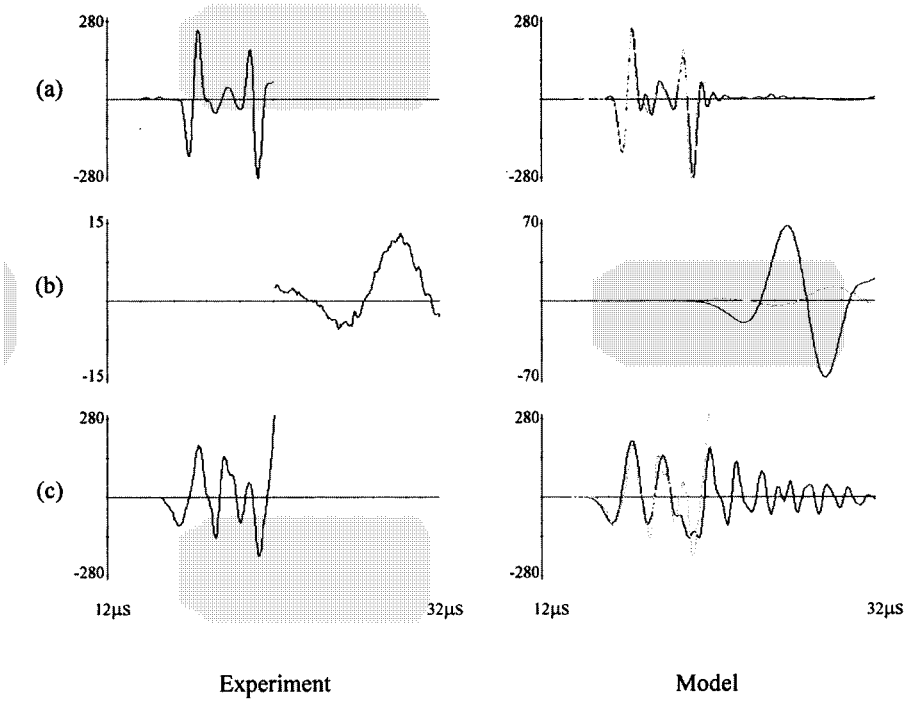

Figure 9
Comparison between experimental waveforms (left) and modelled waveforms (right) for *P*-wave transmission. (a) Solid cylinder. (b) Horizontal fractures with propagation transverse to the fractures. (c) Vertical fractures with propagation parallel to the fractures. The horizontal axis shows time (μs). Experimental waveforms are for voltage (mV), while modelled waveforms are for stress (kPa). Dotted lines are the experimental result superimposed over the model result. The cases for horizontal fractures are shown at different vertical scales due to significant attenuation. Experimental data from PYRAK-NOLTE *et al.* (1990b).

the solid case (9a), although this cannot be quantified simply by the effect on arrival or amplitude. The arrival, amplitude and the total waveform is well reproduced in the model (9c). Wave propagation across the fractures (9b) is significantly delayed and attenuated, with a lower dominant frequency than the solid case (9a). The arrival is approximately 50% later, and the amplitude is attenuated to one twentieth that of the solid case. Similar effects on arrival, amplitude and frequency are observed in the model however to a far lesser degree, where the wave is attenuated to just one quarter that of the solid case. Table 1 compares the experimental and the model times and amplitudes for the first peaks in each *P*-wave experiment, indicating that the most significant difference in the model is that it underestimates the attenuation for wave propagation across the fractures. Models of the shear-wave experiments yielded

Table 1

Amplitude and time for the first peak compared for the different P-wave experiments and for the uniform stiffness model and the stress-dependent stiffness model

	Unfractured		Horizontal fractures		Vertical fractures	
	Ampl. (mV or mm/s)	Time (μs)	Ampl. (mV or mm/s)	Time (μs)	Ampl. (mV or mm/s)	Time (μs)
Experiment	−204	16.9	−4.7	26.3	−102	16.3
Uniform crack stiffness	−191	16.8	−19.8	24.1	−95.5	16.25
(% err)	6%	0.6%	320%	8%	6%	0.3%
Stress-dependent crack stiffness			−8.5	28.8	−97	16.7
(% err)			80%	10%	5%	2%

similar results, where the wave propagation for two different polarizations parallel to the fractures were very well-reproduced, while for wave propagation across the fractures the effects on amplitude, arrival and frequency were consistent with the experiment, although attenuation in particular was too small.

The differences in wave amplitude could indicate the need for an additional dissipative mechanism in the displacement discontinuity model of a fracture to remove mechanical energy from the system. However, it is proposed that the differences result from a non-uniform loading in the experiment which leads to a non-uniform stiffness in the fractures. The biaxial load was applied over a portion of the block. Applying the load of 30 kN to a portion of the block (22 mm by 22 mm), leads to a highly non-uniform stress distribution. The distribution of stress normal to the fractures is shown in Figure 10. Fracture stiffness is related to the compression of a crack and can be expected to vary across the cracks if the normal stress distribution is non-uniform.

A model of stress-dependent fracture stiffness was then developed, based on the hyperbolic joint stiffness relation of BANDIS *et al.* (1983). Introducing this model and applying the loading conditions (details in Appendix A, Section 4), leads to a wide variation of the fracture stiffness in different fractures and within a single fracture. This model leads to considerably lower velocities towards the edges of the block, and greater scattering, resulting in much greater attenuation for wave propagation across the fractures. Figure 11 compares the results of the model of uniform fracture stiffness to those of stress-dependent fracture stiffness, showing that the stress-dependent fracture stiffness leads to substantially greater attenuation of the P waves for propagation across the fractures, while it has little effect on the waves parallel to the fractures. This implies that the displacement discontinuity model can likely account for the effects of fractures on waves without requiring further dissipative mechanisms.

This work highlights the importance of the fracture stiffness in modelling waves through fractures, and hence for modelling waves around deep underground

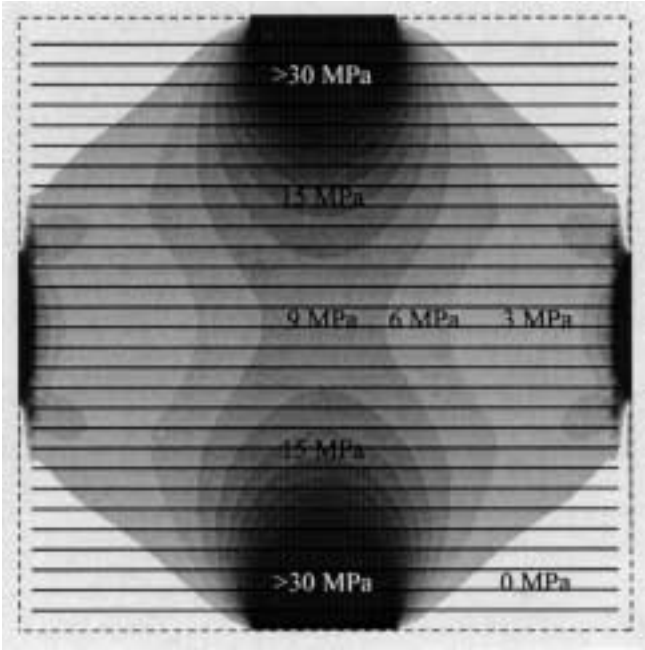

Figure 10
Cross section through the horizontal crack model showing the variation in crack normal stress (σ_{22}). The stress distribution is based on a biaxial load of a 30 kN, applied over the source area, a square region of 22 mm by 22 mm. The block faces are 90 mm by 90 mm.

openings. The fracture stiffness significantly effects the waveforms, delay, amplitude and frequency, causing entirely different behaviour from simply considering fractures as open or closed. In particular the stress dependence of the fracture can be accounted for with a stress-dependent fracture stiffness, and in a non-uniform stress field this stiffness may vary along a single continuous fracture. This has important consequences for modelling fractures around underground openings where stresses are highly non-uniform.

5. Wave Propagation Though in situ Fractures

This section extends the wave-fracture modelling to fractures in *in situ* rock at the surface of a deep tunnel. The data were collected in an acoustic emission experiment encompassing a small volume of rock (approximately 1 m^3) at the surface of the URL Mineby tunnel (CARLSON and YOUNG, 1992, 1993). An acoustic array was installed close to the face of the tunnel. Acoustic emissions were collected over a period of weeks during which there were three 0.5 metre face advances. A number of active velocity scans were also made.

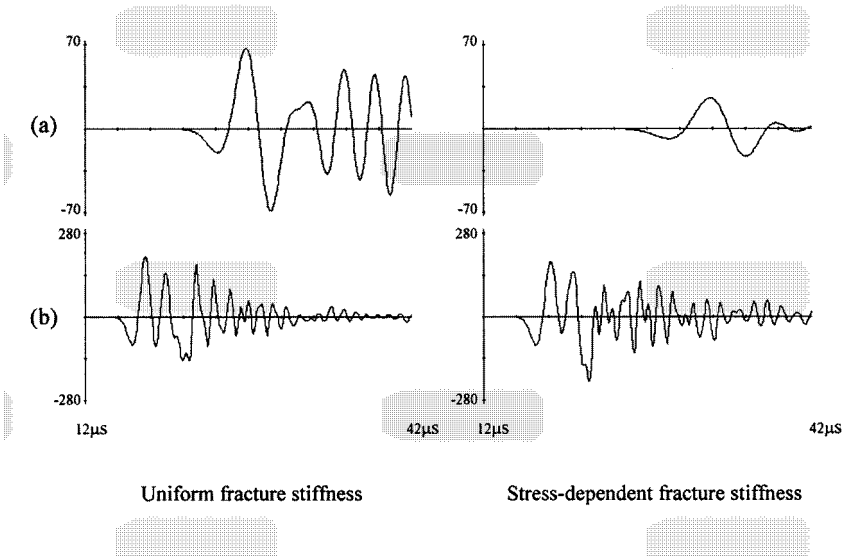

Figure 11
Comparison of waveforms from the uniform fracture stiffness and the stress-dependent fracture stiffness models. (a) *P*-wave response for horizontal fractures (propagation transverse to fractures). (b) *P*-wave response for vertical fractures (propagation parallel to fractures).

Analysis of the experiment (CARLSON and YOUNG, 1992) showed a 12% anisotropy in seismic velocities. The slow direction is orthogonal to the tunnel, while intermediate and maximum velocities are parallel to the tunnel. The anisotropy for compressional wave velocity prior to tunnel advance was calculated as 5810 m/s and 5080 m/s for the maximum and minimum directions, respectively. Crack densities were inferred from the measured seismic velocities and resulting Poisson's ratios, assuming a Poisson's Ratio of 0.2 for the uncracked rock. Crack densities varied with distance from the tunnel wall from 0.12 at the surface to 0.09 at one metre. Most of the recorded emissions were located outside of the array, however changes in velocity and in particular in amplitude were detectable in velocity scans before and after the tunnel advance.

Waveforms from the velocity scans in this experiment are being modelled with explicit representations of the cracking. Besides providing a further measure on how realistically such models capture the real wave behaviour, the modelling seeks to illuminate aspects about the fracturing not directly available from the seismic analysis. In particular the seismic velocities and crack density estimates do not provide a clear link to the actual fracture distribution and size of cracks. Also, since few new emissions were recorded inside the array volume, it is unclear whether changes in the waveforms with tunnel advance are due to new cracking or to a change in the stress field on the existing cracking. This section presents early results in modelling certain velocity scans.

The full acoustic array consisted of 4 parallel boreholes arranged in a diamond pattern. Each borehole contained 5 sensors spaced at approximately 0.2 m intervals, starting at 0.2 m from the tunnel surface. There were 23 sensors in total with 3 mounted on the wall of the tunnel. Sensors were oriented in the boreholes such that they faced the diagonally opposite borehole. The experiment was modelled in three dimensions, with model details given in Appendix A, Section 5. The model used a reduced 8×8 array and the positions of the sensors used are shown in Figure 12. The boreholes were rotated into a diamond pattern as shown with the first borehole at the top. The cube faces are the model boundaries and the element length is 10 mm. The tunnel is circular with a diameter of 3.5 m. The free surface is approximated with a flat surface in the model.

In all the results presented, the source is at sensor 3. A variety of sources were tested by exciting different components of stress and velocity. A good fit was given by simply exciting the normal velocity and recording this at the sensors, allowing for sensor orientation. Rather than trying to model the real source, which contains very high frequencies, the model source is based on the recorded waveforms where most high frequencies are completely attenuated. The amplitude of frequencies above 200 kHz is less than one tenth of the maximum amplitude, which occurs between 25 and 30 kHz. The model source peaks at approximately 60 kHz, and little content above 170 kHz. A typical limit for a fourth-order accurate finite difference scheme and an element size of 10 mm, is a maximum wavelength of 50 mm, which equates to

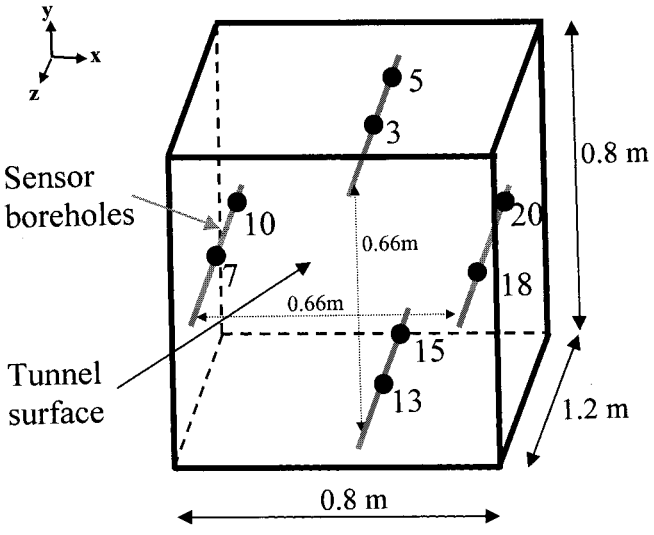

Figure 12
Sketch of the model of the acoustic array. The full array consisted of 4 boreholes, each with 5 sensors spaced at 0.2 m from the tunnel surface. The model used a reduced 8×8 array and the positions of the sensors used are shown. For the model, the boreholes were rotated into a diamond pattern as shown. The model boundaries are also shown.

maximum *P*- and *S*-wave frequencies of 120 kHz and 70 kHz. As a result some numerical dispersion can be observed in these models. The actual source wave shape is shown in Figure 13b, labelled "3:3".

A purely elastic model was constructed using *P* and *S* wavespeeds for the unfractured rock of 5890 m/s and 3425 m/s (YOUNG and COLLINS, 1997). Waveforms are compared with the recorded waveforms in Figure 13 for sensors 3, 7, 13 and 18. These all have wavepaths which are approximately parallel to the tunnel. *P* and *S* waves were found to match well, both in the arrival times and in relative amplitudes, although differences indicate a more complicated source waveshape. Figure 14 compares waveforms for wavepaths which are oblique to the tunnel (sensors 5, 10, 15 and 20). The modelled *P* and *S* arrivals are significantly earlier than the measured waveforms, and have greater amplitude errors than those parallel to the tunnel. This is consistent with the anisotropy shown in the seismic analysis (CARLSON and YOUNG, 1992). The arrival time and amplitude for the different sensors are compared in Table 2, and indicate larger errors in all the oblique paths.

It is proposed that the anisotropy is caused by micro-fracturing predominately parallel to the tunnel. Many models were investigated to account for the anisotropy with a fracture state. The smallest crack which can be represented explicitly in the model is 20 mm. The individual micro-cracks are expected to be of the order of a few

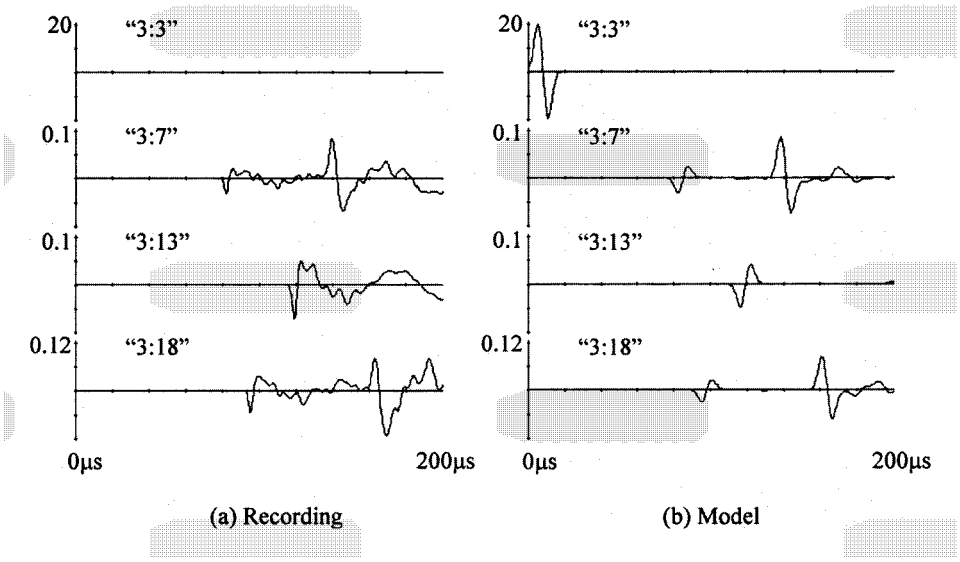

Figure 13
Comparison of measured waveforms with elastic modelled waveforms for sensors 3, 7, 13, 18, with the source at sensor 3. All waveforms are for a 200 μs window. Measured waveforms are in volts. Modelled waveforms are velocity but have been scaled so that amplitudes can be compared. The scaling factor was chosen so that the waveform for sensor 3 matches the amplitude of the experiment.

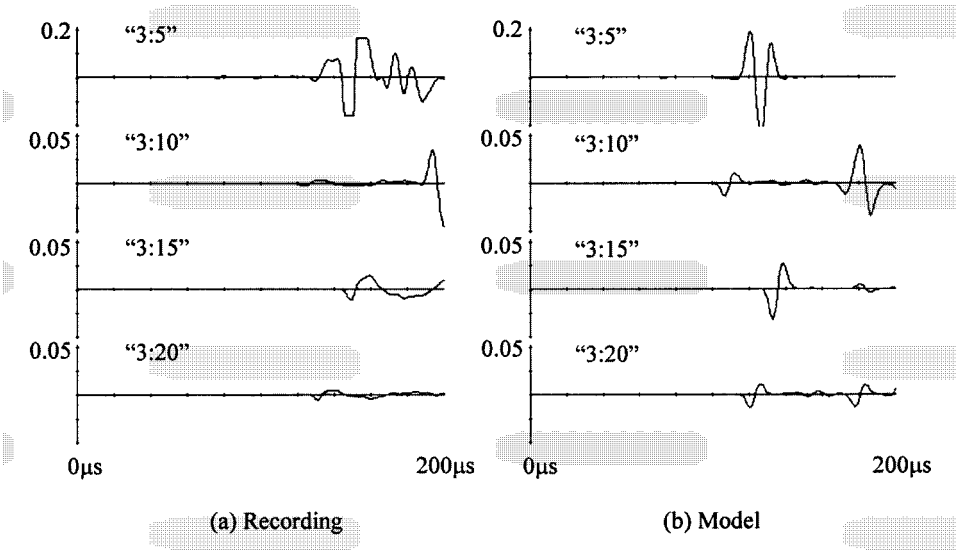

Figure 14
Comparison of measured waveforms with elastic modelled waveforms for sensors 5, 10, 15, 20, with the source at sensor 3. All waveforms are for a 200 μs window. Measured waveforms are in volts. Modelled waveforms are velocity but have been scaled so that amplitudes can be compared. The scaling factor was chosen so that the waveform for sensor 3 matches the amplitude of the experiment. Waveforms are labelled according to the source:receiver pair.

Table 2

Amplitude and time of first arrivals for both P and S waves, compared with the data from the acoustic emission experiment and the elastic model. The paths for sensors 7, 13 and 18 are parallel to the tunnel, while the paths for sensors 5, 10, 15 and 20 are oblique to the tunnel. (The error is expressed as the difference between the modelled and measured values as a percentage of the measured value.)

Sensor	Experiment				Model (%error)			
	P wave		*S* wave		*P* wave		*S* wave	
	Time (μs)	Ampl. (mV)	Time (μs)	Ampl. (mV)	Time (%err)	Ampl. (%err)	Time (%err)	Ampl. (%err)
3								
7	78.6	−31.3	133.5	83.4	−4	1	−1	−2
13	114.9	−72.0	–	–	−4	−31		
18	92.1	−54.6	158.5	83.0	−4	−43	−3	−0
5	73.6	−4.8	131.5	75.9	−11	−31	−13	150
10	117.9	−2.8	188.3	35.4	−15	370	−7	−12
15	142.5	−11.7	–	–	−11	180		
20	125.9	−5.4	–	–	−10	160		

millimetres, therefore it is not possible to represent micro-cracks in the full model. Two approaches were investigated. The first (Fig. 15a) is to use large extensive fractures with surfaces coupled by a fracture stiffness as studied in Section 3. This is based on the hypothesis that the wavelengths are substantially larger than the micro-cracks which can then be seen as the spacing of contacts within a larger crack. The peak frequency in the recorded waveforms corresponds to wavelengths of 200 mm for P waves and 120 mm for S waves.

The second approach is to suggest that the micro-fractures have coalesced into larger micro-fractures, and that these will have the greatest effect on the wave propagation, due to the long wavelengths involved. Crack distributions were generated to give a particular crack density, defined in O'CONNELL and BUDIANSKY (1974) as

$$\varepsilon = (2N/\pi)\langle A^2/P\rangle \ , \tag{16}$$

where the angular brackets denote an average, A is area, P is the perimeter and N is the number of cracks per unit volume, and ε is the crack density. In the models the cracks are rectangular, giving

$$\varepsilon = \frac{1}{\pi V}\sum \frac{A^2B^2}{A+B} \tag{17}$$

where A and B are the side lengths. It was verified that for square cracks this expression gives values in between the values for an inscribed circle and a

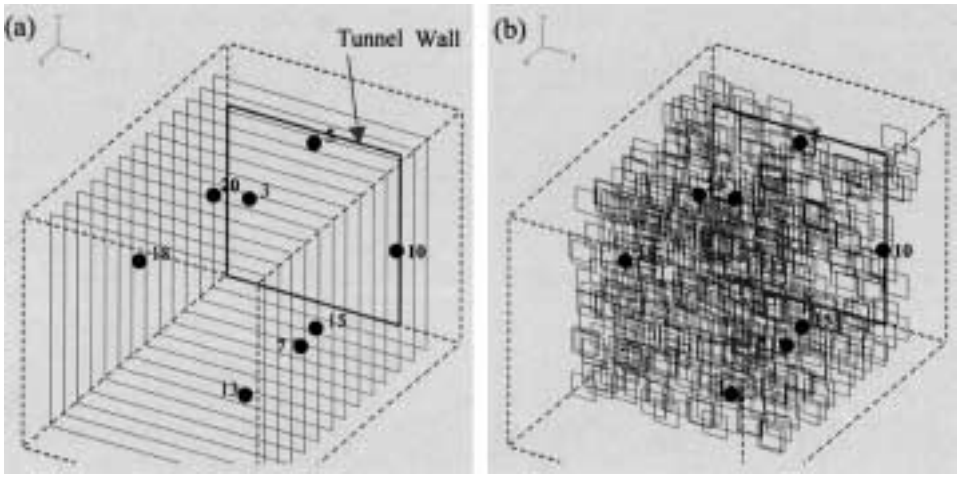

Figure 15
Fracture sets for two different fracture models, also showing the position of sensors and the tunnel wall. (a) Model with large parallel fractures with a normal and shear fracture stiffness of 5*e*12 Pa/m and 2.5*e*12 Pa/m, and an 80 mm spacing. (b) Model with 634 open square cracks with a side-length of 80 mm and a crack density of 0.1.

circumscribed circle, for which expressions are given in O'CONNELL and BUDIANSKY (1974). Figure 15b shows a model with a crack density of 0.1, with 538 square cracks, and an 80 mm side-length.

Figure 16 compares the results of three different fracture models for the wavepath from sensor 3 to sensor 10, indicating the effect on the *P*- and *S*-wave arrivals. The values of these arrivals and amplitudes are also compared in Table 3. The fractures should shift the waveform from the elastic case toward the recorded waveform. The

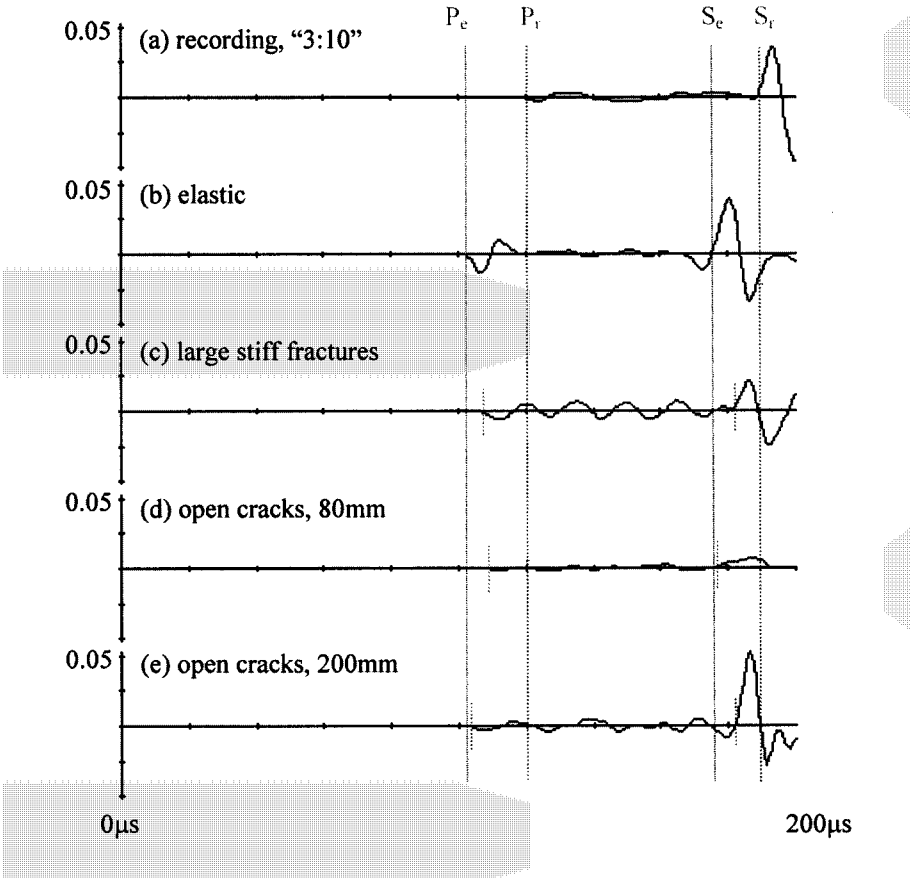

Figure 16

The effects of three different fracture sets on the modelled response for sensor 10, with the source at sensor 3. (a) and (b) are the recording and elastic model from Figure 13. (c) Model with large parallel fractures with a normal and shear fracture stiffness of 5*e*12 Pa/m and 2.5*e*12 Pa/m and an 80 mm spacing. (d) Model with 634 open square cracks with a side-length of 80 mm and a crack density of 0.1. (e) Model with 41 open square cracks with a side-length of 200 mm and a crack density of 0.1. In all cases fractures are parallel to the tunnel surface. The measured waveform is in volts, while modelled waveforms are velocity and have been scaled to the data. P_r, S_r, and P_e, S_e are the *P* and *S* arrivals of the measured waveform and elastic model, respectively.

Table 3

Effect of the different models of fracturing on the amplitude and time of first arrivals for P and S waves, for sensor 10 in the acoustic emission experiment. (The error is expressed as the difference between the modelled and measured values as a percentage of the measured value.)

Model	*P* wave		*S* wave		*P* wave		*S* wave	
	Time (μs)	Ampl. (mV)	Time (μs)	Ampl. (mV)	Time (%err)	Ampl. (%err)	Time (%err)	Ampl. (%err)
Experiment	117.9	−2.8	188.3	35.4				
Elast	100.0	−13.1	174.9	39.6	−15	370	−7	12
Large stiff fractures	103.8	−6.3	181.0	21.5	−12	125	−4	−40
Open 80 mm cracks	103.1	1.3	174.9	7.2	−13	−54	−7	−80
Open 200 mm cracks	100.8	3.0	181.7	52.2	−15	8	−4	47

first fracture model contains large fractures coupled by a fracture stiffness and spaced at 80 mm, and has the greatest effect on the waveform causing significant delays in both the *P* and the *S* arrival. Greater *P*-wave attenuation and delay is still required to match the experiment. The second model contains a random set of open 80 mm square cracks with a fracture density of 0.1, and also causes delayed arrivals, but excessively attenuates the waves. The third model contains a random set of open 200 mm square cracks and causes little delay in the arrivals however with very high attenuation. These observations were consistent when considering the other paths from Figure 14 which are oblique to the tunnel.

These results suggest that the fracture stiffness approach is more likely to account for both the amplitude and arrival effects, perhaps using more densely spaced fractures. The cases of open fractures with a particular density imply that the real openings are considerably smaller than those modelled, as there is a greater effect on attenuation than on arrival.

6. Conclusions

This work has presented a variety of different studies at different scales of the problem but with an overriding theme to provide a measure of how well current models of wave propagation in rock match the real behaviour of waves around deep excavations.

The first section shows some of the difficulties associated with modelling on the true problem-size scale. Although the study was based on a controlled event with an engineered source and *a priori* knowledge, lack of knowledge of the source became an overriding factor in interpreting the model behaviour. The main discrepancy was that

a large shear and surface wave was generated in the model which was not present in the data. Lack of certainty in the complex blast source meant that the differences could not definitely be ascribed to the medium and the interaction with fracturing. Nevertheless important conclusions were noted in that the small calibration blast produced waves travelling close to the skin of the excavation, and modelling these motions proved successful with an elastic medium. Realising goals outlined in the introduction requires that once damaging waves have interacted with the near excavation, the models correctly predict the waves which are transmitted to other parts of the excavation. It is noteworthy then, that modelling the propagation of large amplitude waves along the excavation surface proved significantly less successful than modelling the propagation of small amplitude waves.

A number of conclusions can be made regarding the modelling of fractures. Earlier experimental and theoretical work validating the displacement discontinuity model of a fracture is supplemented by demonstrating numerically that the model not only produces similar frequency-dependent effects on wavespeed and attenuation, but that it can accurately reproduce the waveforms. The work highlights that for realistic wave propagation it is important that models of fractures include a fracture stiffness coupling the surfaces of the fracture, rather than considering fractures as simply open or closed. An important extension is the finding that where the local stress state can vary across a single fracture, that fracture must be modelled with a fracture stiffness that is stress-dependent. This has important implications for modelling the fracture zone around openings where the stress state is highly non-uniform.

Modelling the fractures in *in situ* rock show important preliminary findings. Although the modelling could not practically represent sufficiently small fractures, results did indicate that the sizes modelled were unrealistically large. Such models could give some upper bounds to estimates of fracture size. The fracture stiffness approach seems viable to model a distribution of micro-cracks for wavelengths greater than their separation. A two-part approach may be possible where the data is matched with a distribution of macro-cracks with fracture stiffness, and more detailed models relate the fracture stiffness to a distribution of micro-cracks.

Acknowledgements

I acknowledge Prof. L.J. Pyrak-Nolte for use of her published data, as well as for beneficial discussions. The modelling and developments in this paper have been performed while the first author pursues a Ph.D. degree at Liverpool University in the United Kingdom, under the supervision of Professor R.P. Young, on the subject of seismic wave interaction with underground openings. This work is supported under the project GAP 601, at the CSIR Division of Mining Technology, and is sponsored by SIMRAC (Safety in Mines Research Advisory Committee). This sponsorship is gratefully acknowledged.

Appendix A:

Brief Summary of the Models Used in Each Section

(i) Section 1

The size of the modelled region was $(x, y, z) = (280\text{ m}, 120\text{ m}, 360\text{ m})$. 1.55 million grid-points were used, with a 2 m spacing, and 4th-order spatial accuracy. The elastic parameters were $E = 80$ GPa, $v = 0.2$, $\rho = 2700$ kg/m^3, $c_p = 5738$ m/s, and $c_s = 3514$ m/s. The event modelled was a vertical slip event in the footwall of the pillar. The source centre was 1 m into the pillar, 12 m below the plane of the stope, and 12 m back from the stope face. The region of slip was a square area 28 m by 28 m extending upwards to the plane of the stope and to the stope face. The rupture was propagated from the centre at 3000 m/s. The stress drop at a point was 9.35 MPa, and occurred over 2 ms. Further information pertinent to tabular mining layouts and associated rockbursts can be found in HANDLEY *et al.* (1997), MALAN (1999), or JAGER and RYDER (1999).

(ii) Section 3

The size of the modelled region was $(x, y, z) = (14\text{ m}, 12\text{ m}, 38\text{ m})$. 0.8 million grid-points were used, with a 0.2 m spacing and 4th order spatial accuracy. The elastic parameters were $E = 80$ GPa, $v = 0.2$, $\rho = 2700$ kg/m^3, $c_p = 5738$ m/s, and $c_s = 3514$ m/s. The tunnel dimension was $(x, y, z) = (3.6\text{ m}, 3.6\text{ m}, 37\text{ m})$. Each blast hole was modelled as a line of pressure propagating at the velocity of detonation of the blast. The experimental blast comprised five blast holes varying in length from 4 m to 7 m, and with a velocity of detonations of 3600 m/s or 3800 m/s, and with the five detonations staggered by 71 μs. The position, dimension and blast parameters for each blast hole are given in HILDYARD and MILEV (1999), for both the main experiment and the calibration blast.

(iii) Section 4

The size of the unfractured model was $(x, y, z) = (90\text{ mm}, 100\text{ mm}, 90\text{ mm})$.The size of the fracture models was $(x, y, z) = (90\text{ mm}, 90\text{ mm}, 90\text{ mm})$. The elastic parameters were $E = 210$ GPa, $v = 0.3$, $\rho = 7800$ kg/m^3, $c_p = 6020$ m/s, and $c_s = 3218$ m/s. The normal and shear fracture stiffness for uniform fracture stiffness models was $k_n = 6e13$ Pa/m and $k_s = 2e13$ Pa/m, respectively. Sources were applied over a 22 mm square region, and the received signal was averaged over a 22 mm square region.

– *P*-wave fracture models used 0.75 million grid-points with a 1 mm spacing and 4th order spatial accuracy. The source excited the vertical stress (σ_{yy}).

– *S*-wave fracture models used 5.96 million grid-points with a 0.5 mm spacing and 4th order spatial accuracy. The source excited shear stress, σ_{xy} or σ_{yz} depending on the polarisation considered.

Coupled models applied a stress of 68 MPa to the source area (a square region of 22 mm) on the *y*-*z* and *x*-*z* faces of the block, based on an experimental biaxial load of 30 kN. The stress-dependent stiffness was modelled as $k_n = a/(a - b(-u_n^{\text{rel}}))^2$, where $-u_n^{\text{rel}}$ is the relative displacement or closure of the two crack surfaces, $a = 1e{-}13$ m/Pa, $b = 4.38e{-}8$ Pa^{-1}, and with $k_s = k_n/3$.

(iv) Section 5

The size of the modelled region was $(x, y, z) = (800 \text{ mm}, 800 \text{ mm}, 1200 \text{ mm})$. 6.25 million grid-points were used, with a 5 mm spacing and 4th order spatial accuracy. The elastic parameters were $E = 76.8$ GPa, $v = 0.245$, $\rho = 2630$ kg/m^3, $c_p = 5890$ m/s, and $c_s = 3425$ m/s. Sources and receivers covered a 10 mm square region, and were modelled as velocity normal to the sensor orientations (i.e. normal to the borehole, and facing inward toward the centre of the array (cf. Fig. 12)). The source wave shape is approximately a "full-wave" pulse over 15 μs, and is constructed from the function $-a\tau e^{-15\tau^2}$, where $a \approx 9.03$, $\tau = t/T$, $T = 15e{-}6$, and t is time in seconds. If the values in the figures are interpreted as 'mm/s', then the source has a maximum amplitude of 20 mm/s. The open crack models consisted of 41 200 mm × 200 mm randomly spaced cracks or 634 80 mm × 80 mm cracks in a volume of 770 mm × 770 mm × 870 mm, equating to a crack density of 0.1. The model with extensive stiff fractures contained 12 fractures with a spacing of 80 mm, and with a normal and shear fracture stiffness of $k_n = 5e12$ Pa/m and $k_s = 2.5e12$ Pa/m, respectively.

References

Adams, G. R. and Jager, A. J. (1980), *Petroscopic Observations of Rock Fracturing Ahead of Stope Faces in Deep-level Gold Mines*, J. South African Inst. Min. Metall. *80*(6), 204–209.

Bandis, S. C., Lumsden, A. C. and Barton, N. R. (1983), *Fundamentals of Rock Joint Deformation*, Int. J. of Rock Mech. *20*(6), 249–268.

Cai, J. G. and Zhao, J. (2000), *Effects of Multuiple Parallel Fractures on Apparent Attenuation of Stress Waves in Rock Masses*, Int. J. Rock Mech. and Mining Sci. *37*(4), 661–682.

Carlson, S. R. and Young, R. P. (1992), *Acoustic Emission and Ultrasonic Velocity Study of Excavation-induced Microcrack Damage in the Mine-by Tunnel at the Underground Research Laboratory*, Internal Report #RP015AECL, pp. 901–907.

Carlson, S. R. and Young, R. P. (1993), *Acoustic Emission and Ultrasonic Velocity Study of Excavation-induced Microcrack Damage at the Underground Research Laboratory*, Int. J. of Rock Mech. *30*(7) 901–907.

Crampin, S. (1981), *A review of wave motion in anisotropic and cracked elastic-media*. In *Wave Motion*, vol. 3, pp. 343–391.

Cundall, P. A. (1992), *Theoretical Basis of the Program WAVE*, Unpublished Internal Report, COMRO (now CSIR Division of Mining Technology, CSIR, South Africa), pp. 1–12.

DAEHNKE, A. (1997), *Stress Wave and Fracture Propagation in Rock*, Ph. D. Thesis, Vienna University of Technology.

Graves, R. W. (1996), *Simulating Seismic Wave Propagaion in 3D Elastic Media Using Staggered-grid Finite Differences*, Bull Seismol. Soc. Am. *86*(4), 1091–1106.

GU, B. L., NIHEI, K. T., and MYER L. R. (1996), *Numerical Simulation of Elastic Wave Propagation in Fractured Rock with the Boundary Integral Equation Method*, J. Geophys, Res. *101*(B7), 15,933–15,943.

HANDLEY, M. F., HILDYARD M. W., and SPOTTISWOODE, S. M. (1996), *The influence of deep mine stopes on seismic waves*, Proc. 2nd North American Rock Mechanics Symposium Montreal, pp. 499–506, 19–21 June, 1996.

HANDLEY, M. F., SELFE, D. A., VIEIRA, F. M. C. C., MACCELARI M. J., and DEDE, T. (1997), *Current Position of Strike Stabilising Pillar and Bracket Pillar Design Guidelines for Deep Level Tabular Orebodies*, J. South African Inst. of Mining and Metall. *97*(3), 103–118.

HILDYARD, M. W., DAEHNKE, A., and CUNDALL, P. A. (1995), WAVE: *A computer program for investigating elastodynamic issues in mining*, Proc. of the 35th US Symp. on Rock Mech., pp. 519–524

HILDYARD, M. W. and MILEV, A. M. (1999), *Modeling seismic wave interaction with a tunnel due to an artificial rockburst*, Proc. 2nd SARES (2nd South African Rock Engin. Symp.) (ed. Hagan, T. O.) pp. 273–280.

HUDSON J. A. (1981), *Wave Speeds and Attenuation of Elastic Waves in Material Containing Cracks*, Geophys. J. Roy. Astr. Soc. *64*, 133–150.

JAGER, A. J. and RYDER, J. A., *A Handbook on Rock Engineering Practice for Tabular Hard Rock Mines*, (published by The safety in Mines Research Advisory Committee (SIMRAC), Johannesburg, South Africa, 1999).

KOUZNIAK, N. and ROSSMANITH, H. P. (1998), *Supersonic Detonation in Rock Mass – Analytical Solutions and Validation of Numerical Models – Part 1: Stress Analysis*, FRAGBLAST (Journal) *2*(4), 449–486

LEVANDER, A. R. (1988), *4th-order Finite-difference P-SV Seismograms*, Geophys. *53* (11), 1425–1436.

LIU, E. R., HUDSON, J. A., and POINTER, T. (2000), *Equivalent Medium Representation of Fractured Rock*, J. Geoph. Res. *105*(B2), 2981–3000.

LYSMER, J. and KUHLEMEYER, R. (1969), *Finite Dynamic Model for Infinite Media*, J. Eng. Mech., ASCE *95* (EM4), 859–877.

MADARIAGA, R. (1976), *Dynamics of an Expanding Circular Fault*, By. Seismol. Soc. Am. *66*(3), 639–666.

MALAN, D. F. (1999) *Time-dependent Behaviour of Deep Level Tabular Excavations in Hard Rock*, Rock Mech. Rock Eng. *32*(2), 123–155.

MENDECKI, A. J. (1993), *Real time quantitative seismology in mines, keynote lecture* In Proc. 3rd Int. Symp. *Rockbursts and Seismicity in Mines* (ed. Young, R. P.), (Balkema, Rotterdam 1993) pp. 261–266.

MILEV, A. M., SPOTTISWOODE, S. M., HILDYARD M. W., RORKE, A. J., and FINNIE, G. J. (2000), *Simulated Rockburst – source design, seismic effect and damage*, Proc. of the 4th North American Rock Mech. Symp, July 31–August 3, 2000, Seattle. U.S.A.

MYER, L. R., HOPKINS, D., PETERSON, J. E., and COOK, N. G. W., *Seismic wave propagation across multiple fractures*. In *Fractured and Jointed Rock Masses* (eds. Myer, L. R., Cook, N. G. W., Goodman, R. E., and Tsang, P.), (Balkema, Rotterdam 1995) pp. 105–109.

NAPIER, J. A. L., DAEHNKE, A., DEDE, T., HILDYARD, M. W., KUIJPERS, J. S., MALAN, D. F., SELLERS E. J., and TURNER, P. A. (1997), *Quantification of Stope Fracture Zone Behaviour in Deep Level Gold Mines*, J. South African Inst. Min. Metall. *97*(3), 119–134.

O'CONNELL, R. J. and BUDIANSKY, B. (1974), *Seismic Velocities in Dry and Saturated Cracked Solids*, J. Geophys. Res. *79*, 5412–5426.

PYRAK-NOLTE, L. J., MYER, L. R., and COOK, N. G. W. (1990a), *Transmission of Seismic Waves Across Single Natural Fractures*, J. Geophys. Res. *95*(B6), 8617–8638.

PYRAK-NOLTE, L. J., MYER, L. R., and COOK, N. G. W. (1990b), *Anisotropy in Seismic Velocities and Amplitudes from Multiple Parallel Fractures*, J. Geophys. Res. *95*(B7), 11,345–11,358.

REDDY, N. and SPOTTISWOODE, S. M. (2000), *The Influence of Geology on a Simulated Rockburst Experiment*, J. South African Inst. of Min. Metall, submitted.

SAYERS, C. M. and KACHANOV, M. (1991), *A Simple Technique for Finding Effective Elastic-constants of Cracked Solids for Arbitrary Crack Orientation Statistics*, Int. J. Solids Struct. *27*(6), 671–680.

SCHOENBERG, M. (1980), *Elastic Wave Behaviour Across Linear Slip Interfaces*, J. Acoust. Soc. Am. *68*(5), 1516–1521.

VIRIEUX, J. (1986), *P-SV Wave Propagation in Heterogeneous Media – Velocity-stress Finite-difference Method*, Geophys. *51*(4), 889–901.

YOUNG, R. P., and COLLINS, D. S. (1997), *Acoustic Emission/Microseismicity Research at the Underground Research Laboratory, Canada* (1987–1997), Internal Report #RP037AECL, 1–126.

(Received July 14, 2000, Revised/accepted January 15, 2001)